The International Journal of Advanced Manufacturing Technology (2018) 99:3111–3122
https://doi.org/10.1007/s00170-018-2698-y

ORIGINAL ARTICLE

Mechanical characterization of friction drilled internal threads in AZ91 profiles

Philipp Wittke[1] · Mirko Teschke[1] · Frank Walther[1]

Received: 22 May 2018 / Accepted: 11 September 2018 / Published online: 19 September 2018

Abstract

In this study, the influence of friction drilling tool pre-heating on mechanical properties of chipless manufactured internal threads in thin-walled AZ91 magnesium casting alloy profiles is investigated. In this context, the influence of manufacturing processes on microstructure and the resulting fracture behavior during mechanical loading are in focus for the determination of failure mechanisms. Two batches were investigated, whereas specimens were manufactured without and with pre-heating the friction drilling tool before manufacturing. The mechanical properties were determined in tensile and fatigue tests in tensile loading range. The mechanical results were correlated with the profile qualities in form of computed tomography analyses and hardness mappings. Light and electron microscopic investigations of fractured surfaces were performed to analyze the fracture behavior in cyclic tests. Process-related and stress-related work hardening effects were determined at the edge area of the threads. Differences in fracture behavior under quasi-static and cyclic loads were determined. Turns of internal threads connected to the threaded rod were sheared off in tensile tests without visible cracks on the exterior surface of the flat profile specimens, whereas cyclically tested specimens provided fractured surfaces for fractographic failure analyses. Crack initiation at thread root and two stages of crack propagation until complete failure due to overload fracture were investigated. Pre-heating of the friction drilling tool during manufacturing of the threads had no influence on quasi-static and fatigue properties, respectively.

Keywords Magnesium casting alloy AZ91 · Friction drilling · Thread forming · Internal thread · Quasi-static properties · Fatigue properties

1 Introduction

Magnesium alloys provide various application possibilities due to their low density and good casting and machining behavior. They have been established for saving material, energy, and costs as well as for weight reduction of components and are used in many fields of technical engineering, especially in automotive industry, as mentioned by Kulekci [1] or Muttana [2, 3]. Advantages are, e.g., carriages of relative high cargo loads with low vehicle weights and high maximum velocities with reduced fuel consumption. By reducing the weight of frame-structure elements, the functionality must be obtained. Therefore, magnesium alloys are often used, that ensure high stiffness at minimal weight.

Friction drilling processes are used to generate high strength threads in lightweight profiles, as investigated in Miller et al. [4, 5]. For the conventional application, a fast rotating tool penetrates perpendicular into the profile wall, whereby bushings are formed chipless in feed direction without additional material input, as described by Engbert et al. [6]. Subsequently, heavy duty threads with increased usable thread depths can be generated chipless by means of thread forming so that more flanks of the internal thread are usable [6]. Nutless bolted joints can be realized for applications with one-sided accessibility. Plastic deformation and heat development followed by rapid cooling during the thread manufacturing process lead to microstructural changes in the edge area of the internal threads that affect the mechanical properties, e.g., work hardening. Therefore, the process parameters, e.g., feed, have a significant influence on the properties and microstructure. The parameters should be chosen to maximize the load capacity of the internal threads. During mechanical loads, a multi-axial stress state leads to maximum loads in the thread root.

✉ Philipp Wittke
philipp.wittke@tu-dortmund.de

[1] Department of Materials Test Engineering (WPT), TU Dortmund University, Baroper Str. 303, 44227 Dortmund, Germany

The most common investigated materials for conventional friction drilling process are aluminum alloys [4–25] and steels [4, 11–13, 26–33]. Besides the influence of spindle speed and feed rate on torque and thrust force [7–9, 15], investigations concerning different materials [11–13, 16] and variations in wall thicknesses were performed [11, 12, 17]. Gopichand et al. carried out numerical investigations on process-related stress and strain distributions and deformation behavior [18]. Eliseev et al. performed microstructural investigations and hardness tests without process parameter variations [22–24]. For machining of steels, tool coating [26, 29] and tool geometry [28, 30, 31, 33] were varied to investigate the influence on tool life and tool wear, respectively [26–29]. Krasauskas et al. carried out numerical investigations to compare experimental and simulated process-related workpiece temperature, torque, and thrust force [32]. Brass [13], titanium alloys [4, 34, 35], and nickel-based superalloys [36] are also machinable. Regarding friction drilling of magnesium alloys [5, 20, 37, 38] and the combination of friction drilling and thread forming for aluminum [6, 10, 14, 19, 20] and magnesium alloys [20, 37], only a few publications are available. Miller et al. investigated the effect of workpiece pre-heating, spindle speed and feet rate in conventional friction drilling process of AlSi8Cu3Fe aluminum and AZ91 magnesium casting alloys on torque, thrust force, and bushing shape [5]. All experimental and numerical investigations concerning conventional friction drilling processes deal with process variations (e.g., feed rate, spindle speed) and characterization of the core holes (e.g., roundness deviations, roughness) and tool wear, respectively. No literature is available about investigations on the influence of friction drilling on the mechanical properties, especially fatigue properties, of formed internal threads in friction drilled core holes for magnesium alloys. Concerning mechanical investigations only tensile tests were performed for aluminum alloys [6, 10, 14].

An innovative friction drilling application was investigated by Biermann et al. for AlSi10Mg aluminum casting [21, 25], AZ31 magnesium wrought [37] and AZ91 magnesium casting alloys [38], where the cross-sectional area of thin-walled profiles were machined. The authors of this study already investigated the quasi-static and cyclic deformation behavior of innovative friction drilled and formed internal threads in AlMgSi0.5 [19] and AlSi10Mg aluminum and AZ31 magnesium alloys [20]. In this study, internal threads are also manufactured by means of the innovative front face friction drilling process. The aim is the characterization of the quasi-static and cyclic deformation behavior of formed internal threads from AZ91 casting alloy at room and elevated temperature and the behavior correlation with the profile qualities and changes in microstructure. Newly developed evaluation and testing methods are presented to investigate the influence of friction drilling tool pre-heating on the mechanical properties. Furthermore, knowledge about fracture behavior under quasi-static and cyclic loads is generated that leads to understanding of process-structure-property-relationship.

2 Material and specimen preparation

The chemical composition of magnesium alloy AZ91 used for specimen preparation is given in Table 1. The values were determined by an optical emission spectrometer. The limiting values for alloying elements and impurities, respectively, are also given as reference according to DIN EN 1753. All elements are in the range according to the standard.

Figure 1 illustrates the microstructure of AZ91 in as cast condition (before manufacturing) as cross-sectional scanning electron micrograph (**a**). The EDX-analysis (**b**–**f**) gives some indication of the constituents. The chosen material in cast condition has primary alpha-Mg matrix, eutectic precipitates of alpha-Mg and beta-$Mg_{17}Al_{12}$ phase, as reported by Zhang et al. for non-equilibrium cast structure of Mg-Al-Zn alloys [39]. Small amounts of Al_8Mn_5 and $Al_{11}Mn_4$ were observed.

Internal threads were manufactured by the Institute of Machining Technology (ISF), TU Dortmund University. The core holes and M6 internal threads were drilled on a machining center (Grob, BZ 40 CS) with three synchronic axes, a CNC path control system (Siemens, Sinumerik 840D) and a horizontally arranged main spindle with a maximum rotational speed of $n = 24{,}000\ \mathrm{min}^{-1}$ including a tool holder system (HSK 63). A peripheral speed of $v_u = 40$ m/min and a feed speed of $v_f = 15$ mm/min were used for the friction drilling process in flat profile specimens. Two batches were investigated, whereas specimens from batch "a" were manufactured without pre-heating the friction drilling tool. In the case of batch "b", the tool was pre-heated (initial tool temperature $T = 200$ °C) before manufacturing using a portable induction system, as reported by Biermann et al. [21, 25, 38]. Pre-heating of the friction drilling tool was varied between 150 and 300 °C. Best results regarding the bore quality occurred at 200 °C [38]. The nominal diameter of the subsequent manufactured threads was $d = 6$ mm and the wall thickness of the specimens was $t = 6$ mm. Thread forming was conducted with a peripheral speed of $v_c = 40$ m/min, whereby the feed was determined by the control. The used geometry for flat profile specimens including the position of the M6 internal thread is schematically shown in Fig. 2. The bottom of the hole represents the cone angle of the conical region of friction drilling tool ($\beta_{FD} = 34°$). The wall thickness of flat profile specimens is representative for fatigue-loaded automotive applications, e.g., for crankcases, engine blocks, or space frames.

3 Testing strategy and experimental setup

The mechanical properties of internal threads in flat profile specimens were investigated to characterize the influence of different process parameters for the manufacturing technique thread forming on the quasi-static and cyclic deformation

Table 1 Chemical composition of magnesium alloy AZ91 (wt.-%)

	Mg	Al	Zn	Mn	Si	Fe	Cu	Ni	Others
DIN EN 1753	Bal.	8.3–9.7	0.35–1.0	≥ 0.1	≤ 0.10	≤ 0.005	≤ 0.030	≤ 0.002	≤ 0.01
AZ91	Bal.	8.91	0.57	0.2	0.021	0.0048	< 0.001	< 0.002	≤ 0.01

behavior. Tensile tests and fatigue tests in form of constant amplitude tests (CAT) in tensile loading range were performed and microstructurally evaluated. The maximum loads determined in quasi-static investigations and the lifetimes determined in fatigue tests were compared to quantify the process parameter-related influences on the mechanical properties of the manufactured specimens.

After the mechanical investigations, the results were correlated with the profile qualities at initial (after manufacturing and before mechanical testing) and tested conditions.

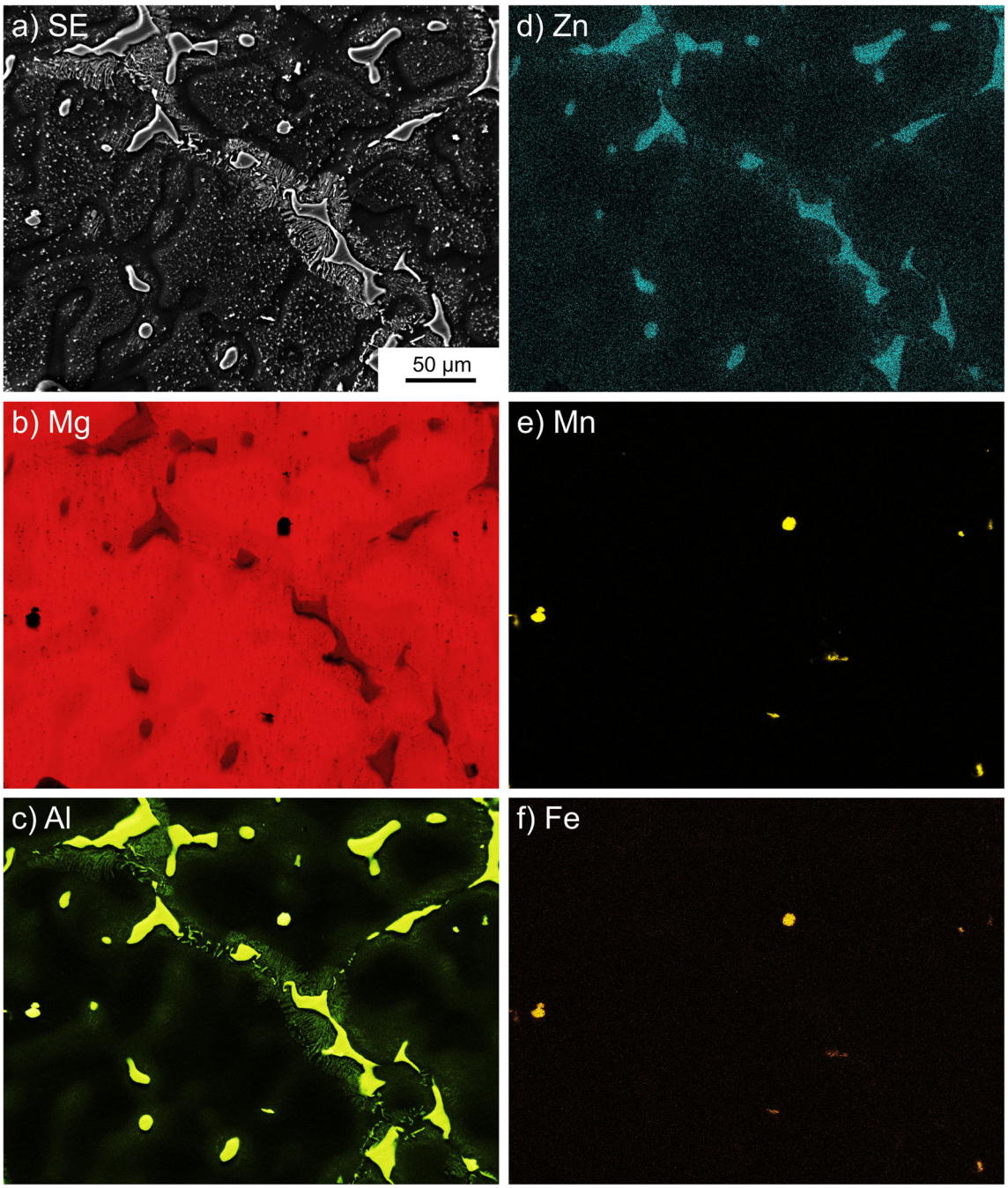

Fig. 1 EDX-mapping, AZ91 as cast

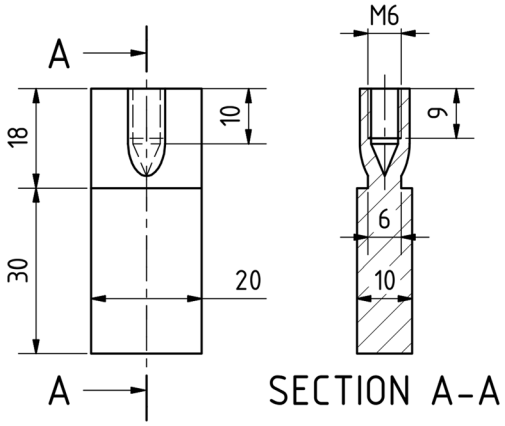

Fig. 2 Geometry of flat profile specimen

Longitudinal and cross sections from computed tomography (CT) and microstructural analyses, respectively, and microhardness mappings were analyzed. The different section views are illustrated in Fig. 3 in top view. The fractured surfaces of flat profile specimens tested in constant amplitude tests were investigated in a scanning electron microscope.

The mechanical investigations were carried out at room temperature on a servohydraulic fatigue testing system (Schenck PC63M, with Instron 8800 control unit) with a maximum load of 63 kN. Tensile tests were also performed at $T = 110$ °C with standard specimen geometries according to DIN 50125 ($d_0 = 6$ mm) and flat profile specimens. Mechanical extensometers were applied to the specimen's surface for strain measurement ($l_{0,RT} = 10$ mm, $l_{0,HT} = 25$ mm). A threaded steel rod M6 in strength class 12.9 was used as counter thread. The magnesium specimens were connected with a steel counter holder to the threaded rod. The threaded rod was screwed four turns into the test specimen, whereby a defined screw-in depth of $H = 4$ mm was realized.

The experimental setup for the mechanical investigations is illustrated in Fig. 4. The tensile tests were carried out strain-controlled with a deformation rate of $\dot{\varepsilon} = 2.5 \cdot 10^{-4}$ 1/s until the abort criteria $F_{ac} = 10\%\ F_{max}$ (90% loss of maximum force F_{max}) and $\varepsilon_{max} = 3\%$, respectively, were reached. In constant amplitude tests, the specimens were loaded with sinusoidal load-time functions at a load ratio of $R = 0.1$ and a frequency

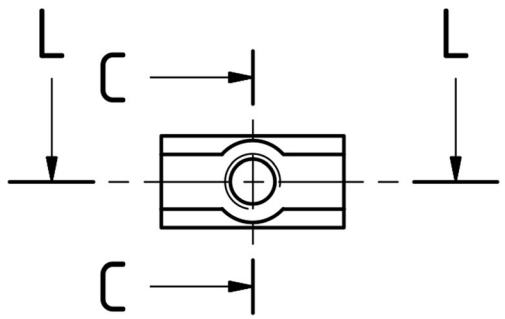

Fig. 3 Definition of section views in top view (L longitudinal section; C cross section)

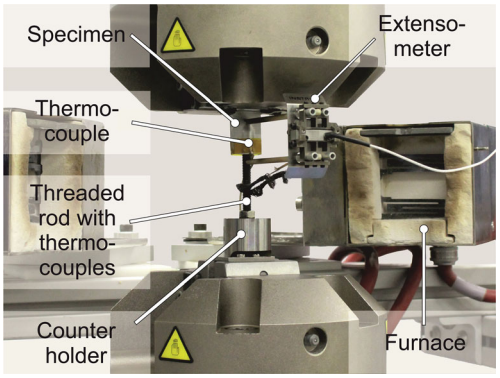

Fig. 4 Experimental setup with integrated flat profile specimen for mechanical investigations

of $f = 10$ Hz until 1E7 cycles. Deformation-induced changes in strain and temperature were determined load- and cycle-dependently as material responses, based on investigations from Ebel-Wolf et al. [40] and Walther [41]. The specimens were assembled analogous to the tensile test, whereby the extensometer was used to measure fatigue-related strain parameters. To measure the change in temperature K-type miniature-thermocouples were utilized, whereby the junctions were installed through drilled holes and milled notches in the threaded rod to get access to the stressed areas of the thread flanks, as introduced by Wittke et al. [20]. Moreover, the miniature-thermocouples were used for temperature control in tensile tests for flat profile specimens at elevated temperature.

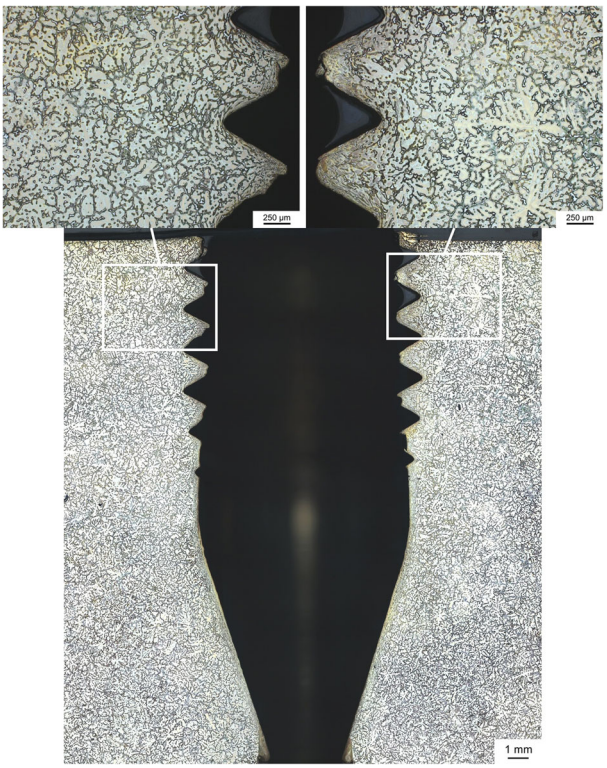

Fig. 5 Longitudinal section of flat profile specimen, AZ91(a) initial state

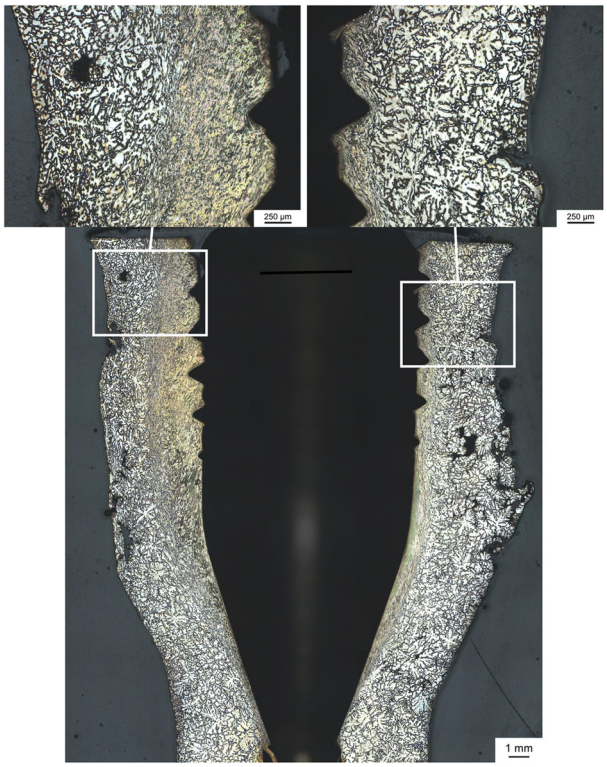

Fig. 6 Cross section of flat profile specimen, AZ91(a) initial state

4 Results and discussion

4.1 Microstructure and thread quality

Light microscopic images from longitudinal and cross sections of etched AZ91(a) flat profile specimens in initial state are shown as overview and detail in Figs. 5 and 6, respectively.

All turns are formed well, whereby characteristic claw shapes due to thread forming process and resulting thread flanks are pronounced differently between individual turns (Fig. 5). Small geometrical differences are supposed to have little impact on mechanical properties in contrast to incompletely formed turns. Rugged surfaces can be observed in the outer area of the cross section and cavities, which extend along the brittle beta-phase (Fig. 6). This behavior can be observed for both batches. The influence of the near-surface damaged areas on the mechanical properties of the threads is not clarified. Those surfaces can be unfavorable for specific technical applications, e.g., automotive parts. In addition to poor-quality suggesting appearance (esthetical reasons), the surfaces are prone to corrosive attack and hard to clean. Corrosive attack can decrease mechanical properties due to decreasing structural integrity based on material loss. Furthermore, the cross section shows incompletely manufactured turns due to oval forms of the core holes, as reported for AlSi10Mg flat profile specimens by Wittke et al. [20]. Since the diameter of the core hole is larger in cross direction after friction drilling process, there is less material available for thread forming process than in longitudinal direction. In incompletely formed turns, the threaded rod is not or only partly engaged in cross direction. The microstructure along the thread flank is deformed due to the thread forming process.

Figures 7 and 8 show longitudinal and cross sections from non-destructive computed tomography analyses of AZ91(a) and AZ91(b) flat profile specimens in initial state as overview (a) and detail (b). The analyses were performed on an X-ray and CT testing system (Nikon XT H 160). Since in mechanical investigations, a screw-in depth of $H = 4$ mm was used, the focus lies on the first four formed turns of the internal threads. The light blue colored area represents the sectional view of the analyzed volume of the hollow space for the first four turns (b). For AZ91(a), a volume of $V_{H=4mm} = 110.0$ mm^3 and for AZ91(b) a 7.3% lower volume of $V_{H=4mm} = 102.0$ mm^3 was determined. The volume of AZ91(a) is higher due to incompletely manufactured turns, as can be seen in longitudinal and cross section (Fig. 7). The turns from AZ91(b) specimen are formed well in longitudinal and cross section (Fig. 8). Incompletely formed turns affect the mechanical properties negatively, since the threaded rod is not or only partly engaged. The qualities of specimens in both batches vary process-related. The results from one scanned specimen and the calculated volume are unrepresentative for all specimens of the entire batch. For mechanical investigations,

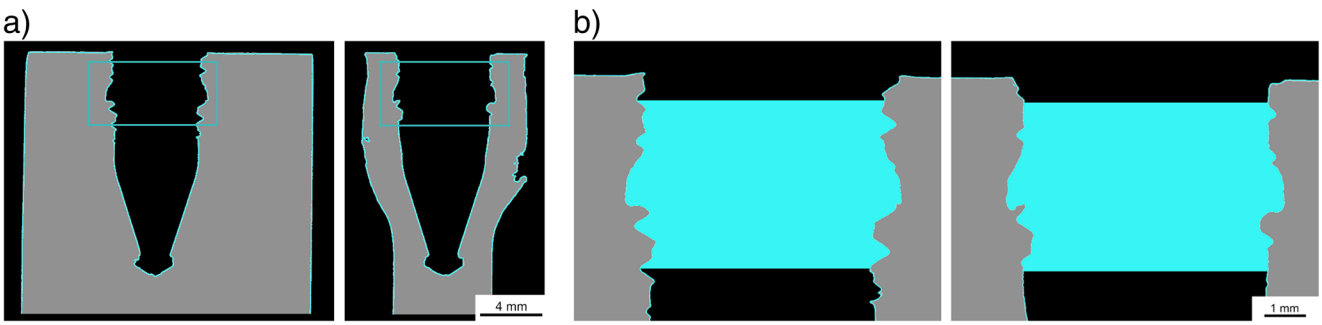

Fig. 7 Longitudinal and cross section from CT analysis of flat profile specimen, AZ91(a) initial state. **a** Overview. **b** Detail

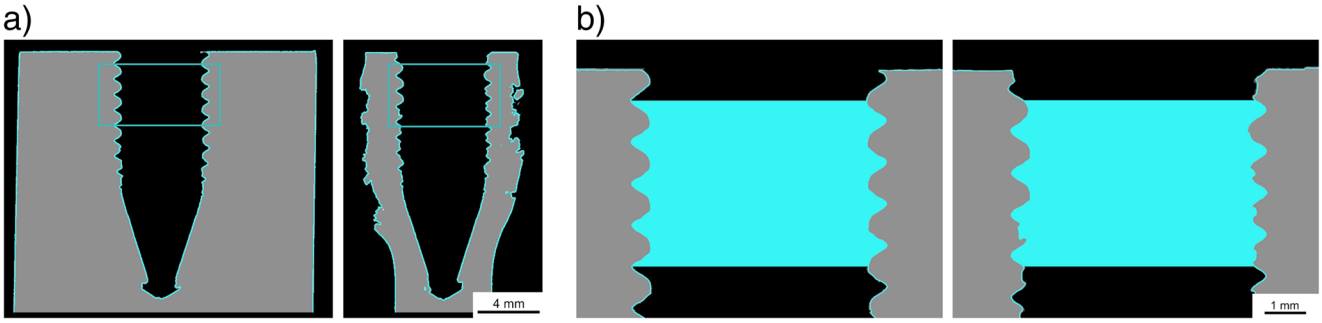

Fig. 8 Longitudinal and cross section from CT analysis of flat profile specimen, AZ91(b) initial state. **a** Overview. **b** Detail

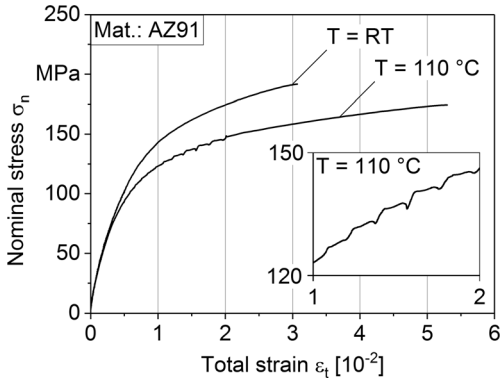

Fig. 9 Characteristic stress-strain curves for quasi-static tensile tests for specimens with standard tensile specimen geometry

only specimens with completely formed turns were used, except the AZ91(a) specimen from Fig. 7 to show the influence of incompletely manufactured turns on quasi-static properties (Fig. 10a).

4.2 Quasi-static properties

The ultimate tensile strength of as-cast AZ91 magnesium alloy was determined by means of tensile tests with standard tensile specimen geometry (DIN 50125—A 6 × 30). Four specimens were tested at each testing temperature. At room temperature, specimens exhibit higher values ($UTS_{RT} = 179 \pm 21$ MPa) than at elevated temperature ($UTS_{110°C} = 165 \pm 22$ MPa). On the other hand total elongation at fracture increases with increased testing temperature.

Representative stress-strain curves for both testing temperatures are illustrated in Fig. 9. Results from literature are repeatable with the used test setup and there is no influence on results for comparable tests with flat profile specimens (Fig. 10). At elevated temperature, a serrated flow curve can be recognized until a total strain of $\varepsilon_t = 2\%$, which corresponds with the threshold for raising the testing speed from $\dot{\varepsilon}_{Le} = 2.5 \cdot 10^{-4}$ 1/s to $\dot{\varepsilon}_{Lc} = 6.7 \cdot 10^{-3}$ 1/s (strain rates according to standard DIN EN ISO 6892-1). The pronounced behavior indicates a Portevin-Le-Chatelier (PLC) effect. Since the PLC-effect depends on strain rate and testing temperature, as reported for AZ91 by Corby et al. [42] and Trojanová et al. [43], respectively, it did not occur at room temperature.

Figure 10 shows force-total strain diagrams from tensile tests for flat profile specimens at $T = \text{RT}$ (a) and $T = 110$ °C (b). After the linear-elastic range, all specimens exhibit maximum forces followed by a decrease with several force drops. The serrated flow curves after reaching maximum forces suggest a PLC-effect analogous to tensile tests for specimens with standard tensile specimen geometry. The decrease in all curves indicates that the flat profile specimens do not fail brittle in contrast to standard tensile specimens. A geometrical effect superimposed by the PLC-effect is assumed, where areas from the threads fail one

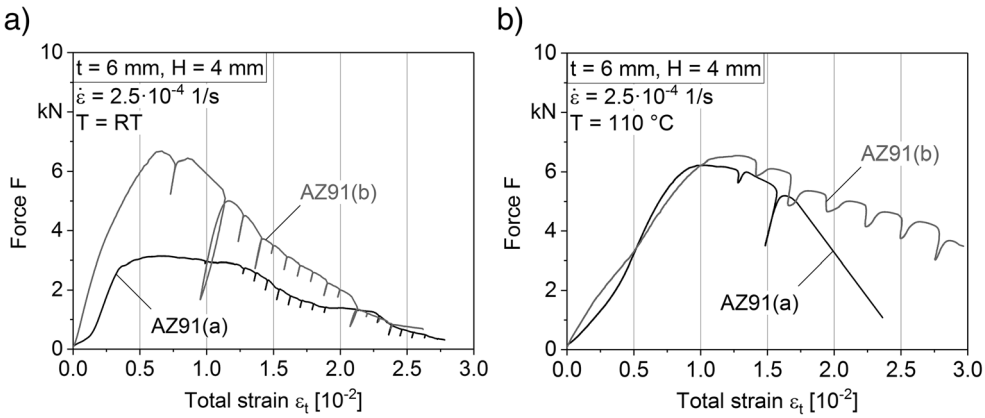

Fig. 10 Force-total strain diagrams for flat profile specimens. **a** $T = \text{RT}$. **b** $T = 110$ °C

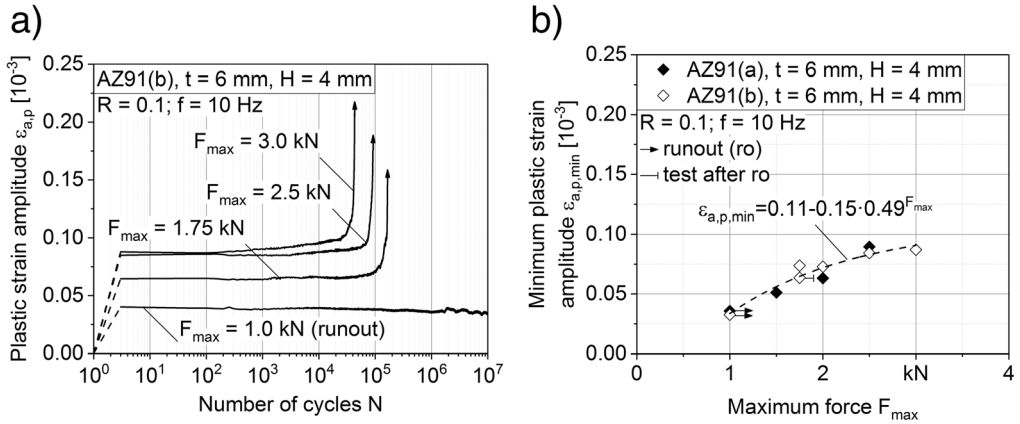

Fig. 11 **a** Cyclic deformation curves for AZ91(b) flat profile specimens. **b** Relationship between minimum plastic strain amplitude and maximum force in constant amplitude tests

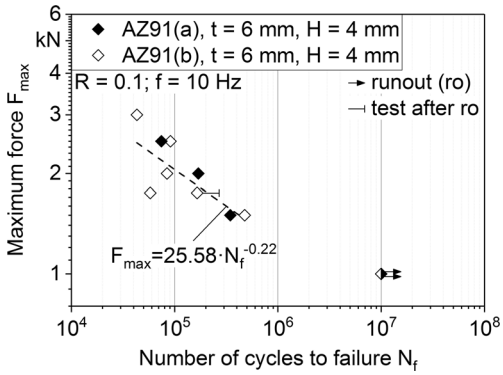

Fig. 12 Woehler curve (S-N curve) for flat profile specimens

after another so that the residual profile decreases with increasing total strain. At $T = 110$ °C, the force drops are less pronounced due to a higher characteristic of the geometrical effect at elevated temperature. The maximum force for AZ91(a) is $F_{max} = 3.12$ kN at a total strain of $\varepsilon_t = 0.61\%$ at room temperature. AZ91(b) exhibits a more than twice as high maximum force $F_{max} = 6.68$ kN at a similar total strain ($\varepsilon_t = 0.66\%$). The low value of AZ91(a) at room temperature is due to incompletely formed turns as shown for the CT-analyzed specimen in Fig. 7, which was used for this test. For tests at elevated temperature, the maximum forces for both batches are nearly the same whereas the total strains at maximum forces are higher compared to results at room temperature ($F_{max} = 6.21$ kN at $\varepsilon_t = 0.97\%$; $F_{max} = 6.54$ kN at $\varepsilon_t = 1.29\%$). In case of AZ91(b), the testing temperature has no influence on maximum bearable loads of the flat profile specimens. On the other hand, the increase in testing temperature leads to an increase of total strain at maximum force and flatter decrease of the slope after reaching maximum forces.

4.3 Fatigue properties

The cyclic deformation behavior of AZ91(b) flat profile specimens is shown in Fig. 11a. Selected deformation curves are plotted for clear presentation. The plastic strain amplitude $\varepsilon_{a,p}$ determined from stress-strain hysteresis loops is plotted as function of the load cycles N. The plastic strain amplitude is nearly constant in all tests, whereby

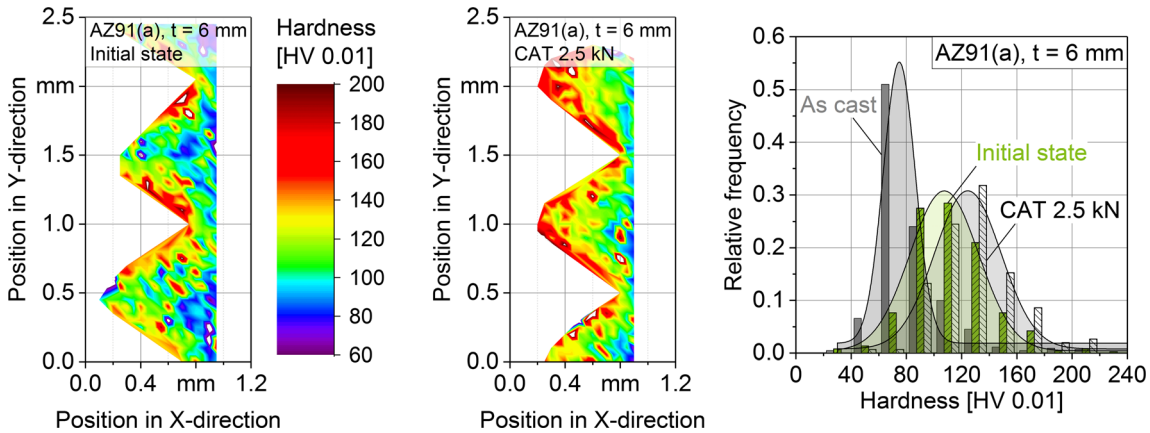

Fig. 13 Micro-hardness mappings and histograms for flat profile specimens, AZ91(a) initial state and after constant amplitude test with 2.5 kN maximum force (CAT 2.5 kN)

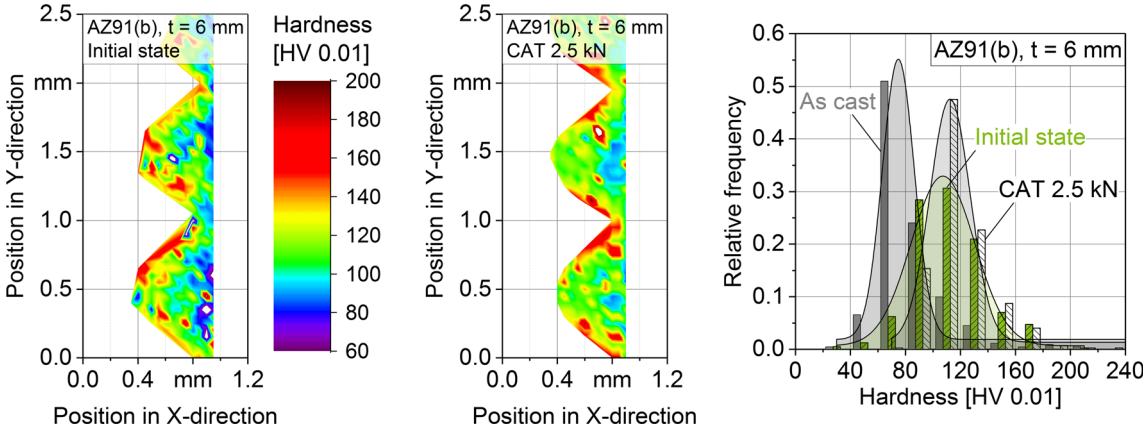

Fig. 14 Micro-hardness mappings and histograms for flat profile specimens, AZ91(b) initial state and after constant amplitude test with 2.5 kN maximum force (CAT 2.5 kN)

higher load amplitudes lead to higher $\varepsilon_{a,p}$ values and lower lifetimes N_f, as reported for AlMgSi0.5 aluminum wrought alloy by Wittke et al. [19]. In curves with $F_{max} > 1.0$ kN, the relative constant strain hardening plateau is followed by an exponential course until failure due to crack initiation and propagation. For the runout (specimen without fracture until fatigue limit 1E7, as described in [44]), the plastic strain amplitude follows a nearly steady progression. Even for relative small differences in number of cycles to failure, a difference for the values in strain hardening plateau is recognizable. In Fig. 11b, the relationship between the minimum plastic strain amplitude $\varepsilon_{a,p,min}$, as representative value for the strain hardening plateau, and maximum forces in constant amplitude tests is described. An exponential correlation was found as described in Eq. (1).

$$\varepsilon_{a,p,\min} = 0.11 - 0.15 \cdot 0.49^{F_{max}} \quad (1)$$

The maximum forces F_{max} used in constant amplitude tests are plotted against the number of cycles to failure N_f in a Woehler diagram (S-N diagram) in Fig. 12 to understand the relationship of load level and fatigue life in high cycle fatigue (HCF) range. The lifetimes from cyclic deformation curves (Fig. 11a) are included. Between the two tested charges, no significant difference can be observed. It can be concluded that pre-heating of the friction drilling tool during manufacturing of the threads has no influence on the fatigue properties, analogues to the quasi-static properties. One specimen was tested for each maximum force and batch. For AZ91(b), two specimens were tested at $F_{max} = 1.75$ kN. A relatively low scatter can be observed, though a small number of specimens was tested, which indicates that the manufacturing process leads to reproducible thread qualities. A combined Basquin equation for both batches is given in Eq. (2). Runouts were not included in the regression analysis.

$$F_{max} = 25.58 \cdot N_f^{-0.22} \quad (2)$$

4.4 Work hardening behavior

In Figs. 13 and 14, micro-hardness mappings from longitudinal sections and corresponding histograms for AZ91(a) and AZ91(b) flat profile specimens are shown in initial state and after constant amplitude tests at $F_{max} = 2.5$ kN. Additionally, histograms for the as cast condition are illustrated. Vickers hardness tests were performed on a hardness testing system (Shimadzu HMV-G21) according to standard DIN EN ISO

Table 2 Parameters for micro-hardness distributions from Gaussian function, as cast, initial state and after constant amplitude test with 2.5 kN maximum force (CAT 2.5 kN)

Batch	Condition	Expected value	Standard deviation	Geometric factors		Coefficient of
		μ [HV 0.01]	σ [HV 0.01]	y_0	A [HV 0.01]	determination R^2
AZ91	As cast	74.82	23.24	0.019	15.53	0.97
AZ91(a)	Initial state	107.44	49.76	0.004	18.93	0.98
	CAT 2.5 kN	124.44	48.20	0.008	18.12	0.97
AZ91(b)	Initial state	107.27	46.17	0.007	18.69	0.97
	CAT 2.5 kN	112.42	29.41	0.013	17.03	0.98

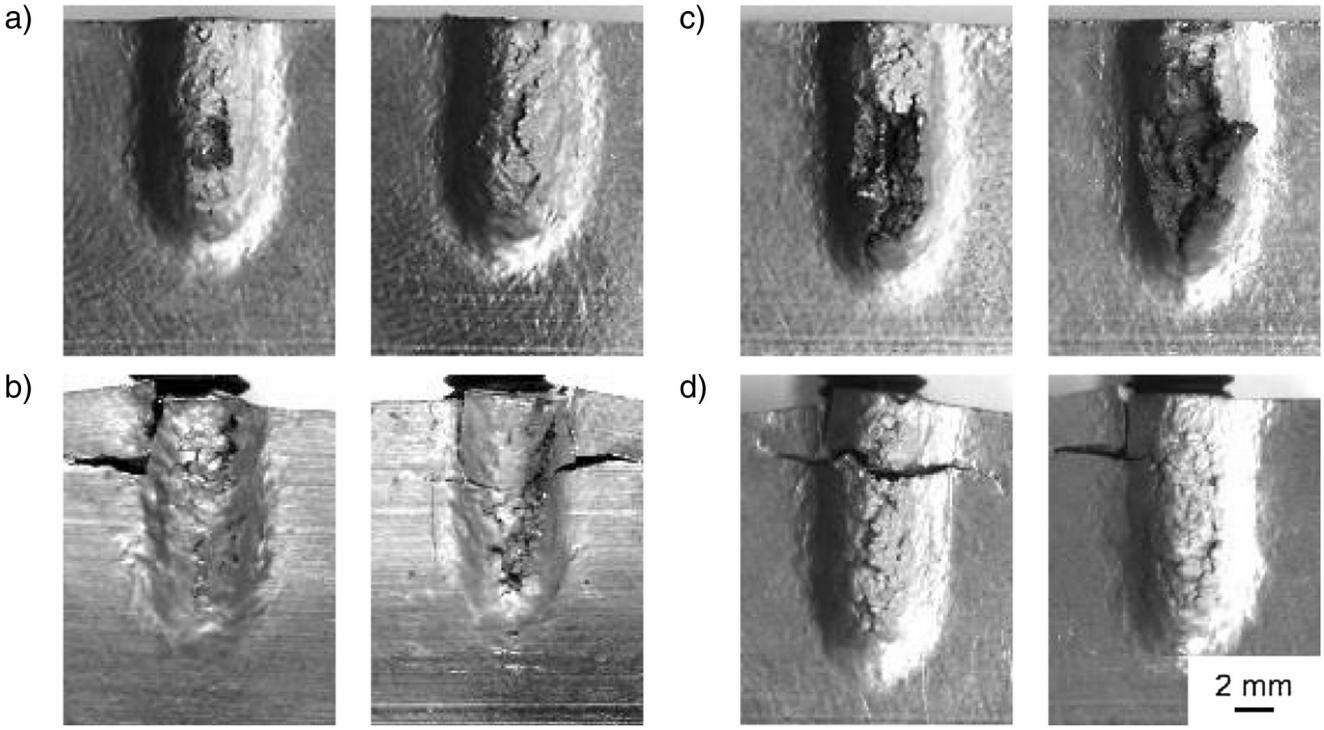

Fig. 15 Outer bore walls of flat profile specimens. **a** AZ91(a) initial state. **b** AZ91(a) after constant amplitude test with 2.5 kN maximum force (CAT 2.5 kN). **c** AZ91(b) initial state. **d** AZ91(b) CAT 2.5 kN

6507-1 with a force of $F = 0.098$ N (HV 0.01) and an indentation time of 10 s. Grids of indentations were arranged in the area of first load-bearing thread flanks. The distance between the centers of the indentations was 50 μm.

The micro-hardness distributions shown in the histograms were classified with Gaussian function as given in Eq. (3), with geometric factors y_0 and A, expected value μ, and standard deviation σ.

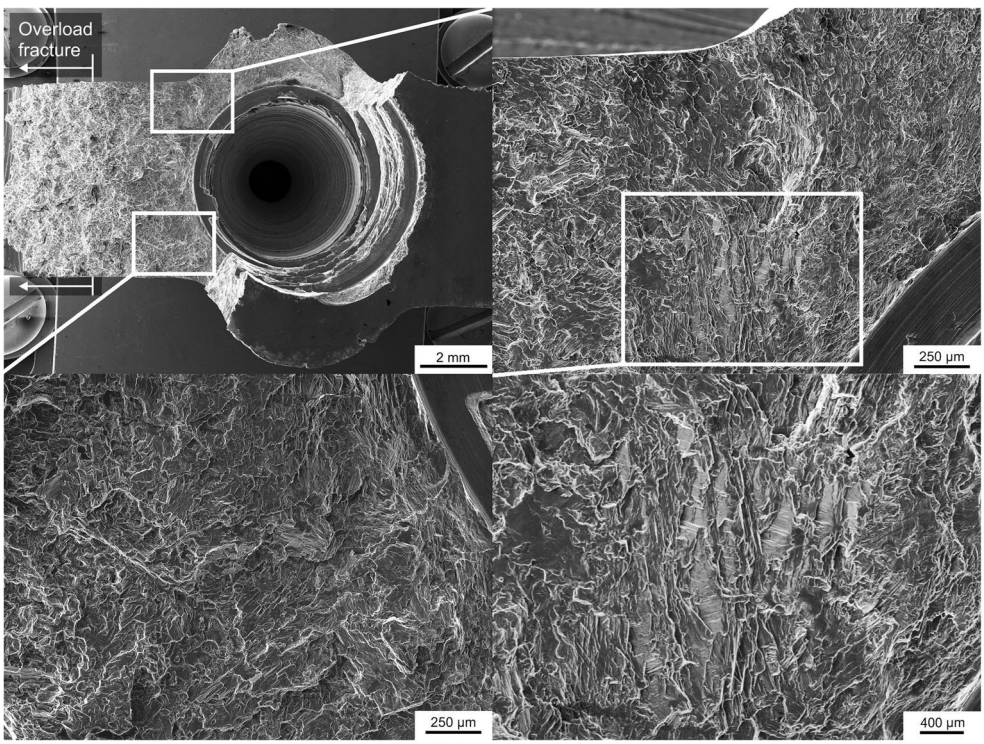

Fig. 16 Fractured surface of flat profile specimen, AZ91(a) after constant amplitude test with 2.5 kN maximum force

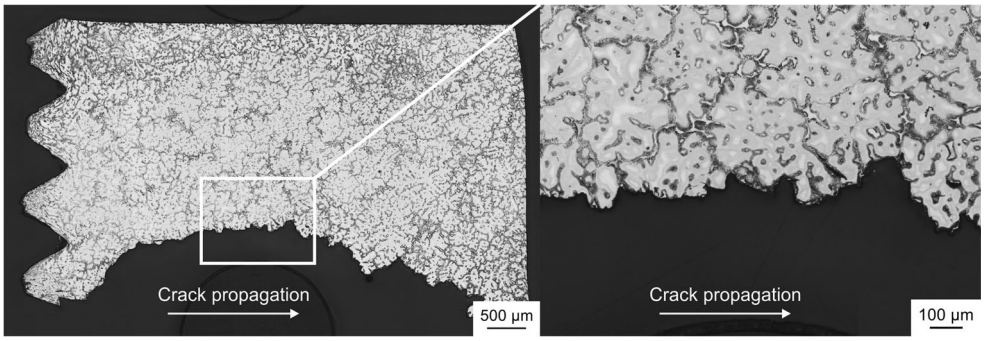

Fig. 17 Longitudinal section of counterpart from fractured surface of flat profile specimen, AZ91(a) after constant amplitude test with 2.5 kN maximum force

$$y = y_0 + \frac{A}{\sigma\sqrt{\pi/2}} e^{-2\frac{(x-\mu)^2}{\sigma^2}} \quad (3)$$

The parameters for micro-hardness distributions are shown in Table 2. As can be seen from coefficient of determination ($R^2 \geq 0.97$), the measured hardness values are normally distributed. The expected value is nearly the same for the initial state for both batches (107 HV 0.01). In comparison to the basic hardness of the AZ91 as cast condition (75 HV 0.01), the initial states of both batches exhibit a 44% higher value. In addition to a process-related work hardening, a stress-related work hardening effect can be determined at the edge area of the threads. The specimen after constant amplitude test exhibits a 16% higher value for batch "a" (124 HV 0.01) and a 5% higher value for batch "b" (112 HV 0.01), respectively, in relation to the initial state. The standard deviation only differs slightly for the two conditions of batch "a" (3%). The standard deviation for the specimen after constant amplitude test for batch "b" is 36% smaller compared to the initial state. For each micro-hardness mapping, different specimens were used, since the measurements were performed on polished longitudinal sections (destructive method). The investigated initial state could not be tested in constant amplitude tests afterwards, which leads to the difference in standard deviations.

4.5 Fracture behavior

Investigations concerning the fracture behavior of flat profile specimens after tensile and constant amplitude tests show differences in terms of failure mechanisms. After tensile tests, no fractured surfaces occur and the threaded rods were not turnable anymore. Deformations between threaded rod and internal threads of the specimens prevent rotational movements after the tests. Turns of internal threads connected to the threaded rod were sheared off in tensile tests without visible cracks on the exterior surface of the flat profile specimens.

In Fig. 15, outer bore walls from two opposite views of AZ91(a) and AZ91(b) flat profile specimens are illustrated. In initial state (a, c), the surfaces exhibit damaged brittle material in the middle of the widened zone. It is assumed that the maximum degree of forming is achieved in the middle of the widened zone during friction drilling process, since the material exhibits the largest displacement there. The extent of process-related damage varies for both AZ91(a) and AZ91(b) specimens, as can be seen for outer bore walls of different specimens after constant amplitude tests at F_{max} = 2.5 kN (b, d). Fractured surfaces were generated with cracks at a distance of about 4 mm from the border of the specimen which corresponds to the screw-in depth of the threaded rod, as reported for AZ31 flat profile specimens after continuous load increase tests by Wittke and Walther [20].

Figure 16 shows SEM images of a fractured surface of an AZ91(a) flat profile specimen after constant amplitude test at F_{max} = 2.5 kN as overview and detail. Fatigue fracture characteristics, like river patterns (top right, bottom left) and striations (bottom right), respectively, indicate that the crack initiates at the thread root due to stress triaxiality and propagates towards the outer areas of the specimen. A brittle transgranular fracture mode can be observed with cleavage facets (bottom right). Fracture mode changes to overload fracture at a distance of about 3 mm from the thread root towards longitudinal direction (top left).

Light microscopic images from longitudinal section of counterpart from fractured surface of AZ91(a) flat profile specimen after constant amplitude test at F_{max} = 2.5 kN are shown as overview and detail in Fig. 17. On the etched surface, two stages of crack propagation can be identified. During mechanical loads, a multi-axial stress state leads to maximum loads in the thread root. Starting with crack initiation at the thread root between the fourth and fifth turn, which corresponds to the screw-in depth of the threaded rod, the crack propagates at an angle of 45° to the loading direction and after approximately 3 mm of crack path normal to the loading direction. After the change in propagation direction, the fracture mode changes from transgranular to intergranular fracture along the beta-phase, which indicates the area of overload fracture. The two fracture modes were also reported in fatigue tests for cylindrical AZ91 specimens by Eisenmeier et al. [45].

5 Conclusions and outlook

Quasi-static and cyclic mechanical properties of internal threads manufactured by friction drilling and subsequent thread forming in thin-walled AZ91 casting alloy were investigated. The mechanical results were correlated with the profile qualities in form of computed tomography analyses and hardness mappings. Two batches were manufactured without and with pre-heating the friction drilling tool before manufacturing. The results can be summarized as follows:

Thread quality

- Rugged surfaces in outer area of cross section and cavities, which extend along brittle beta-phase.
- Incompletely manufactured turns in cross section due to oval forms of core holes.
- Process-related variations in qualities of specimens in both batches.

Mechanical properties

- No influence of pre-heating of friction drilling tool on quasi-static and fatigue properties, respectively.
- Serrated flow curves after reaching maximum forces in tensile tests.
- Geometrical effect superimposed by PLC-effect, where areas from threads fail one after another so that residual profile decreases with increasing total strain.
- No influence of testing temperature on maximum bearable loads.
- Relative constant strain hardening plateaus for plastic strain amplitudes in fatigue tests.
- Difference for values in strain hardening plateau even for small differences in lifetime.
- Low scatter in Woehler curve indicates that manufacturing process leads to reproducible thread qualities.

Work hardening/fracture behavior

- Process-related and stress-related work hardening effect at edge area of threads.
- No fractured surfaces and threaded rods not turnable anymore after tensile tests.
- Turns connected to threaded rod sheared off without visible cracks on exterior surface.
- Crack initiation at thread root between fourth and fifth turn occurs in cyclic tests.
- Two stages of crack propagation until complete failure due to overload fracture.

The results provide the basis for further studies, e.g., to analyze the failure mechanisms in tensile and fatigue tests. To compare the different failure mechanisms during and after mechanical loading, computed tomography investigations before and after the tests and in defined stress conditions are planned.

Acknowledgements The authors thank the colleagues S. Hannich and Prof. D. Biermann at Institute of Machining Technology (ISF), TU Dortmund University, for the provision of the friction drilled internal threads in the context of an excellent scientific cooperation within this research project.

Funding information This study received financial support from the Deutsche Forschungsgemeinschaft (DFG, German Research Foundation) within the research project "Holistic development and characterization of an efficient manufacturing of detachable joints for aluminium and magnesium lightweight materials" (WA 1672/11-1).

References

1. Kulekci MK (2008) Magnesium and its alloys applications in automotive industry. Int J Adv Manuf Technol 39:851–865. https://doi.org/10.1007/s00170-007-1279-2
2. Muttana SB, Aggarwal D (2015) Prospects of magnesium for automotive lightweighting applications - part I. Auto Tech Rev 4(3): 18–23. https://doi.org/10.1365/s40112-015-0872-2
3. Muttana SB, Aggarwal D (2015) Prospects of magnesium for automotive lightweighting applications - part II. Auto Tech Rev 4(4): 18–23. https://doi.org/10.1365/s40112-015-0894-9
4. Miller SF, Blau PJ, Shih AJ (2005) Microstructural alterations associated with friction drilling of steel, aluminum, and titanium. J Mater Eng Perform 14(5):647–653. https://doi.org/10.1361/105994905X64558
5. Miller SF, Tao J, Shih AJ (2006) Friction drilling of cast metals. Int J Mach Tool Manu 46(12–13):1526–1535. https://doi.org/10.1016/j.ijmachtools.2005.09.003
6. Engbert T, Biermann D, Zabel A (2010) Internal threads for thin-walled sections. ICAA12, Proc of the 12th International Conference on Aluminium Alloys, pp 601–606
7. Gopal Krishna PV, Kishore K, Satyanarayana VV (2006) Some investigations in friction drilling AA6351 using high speed steel tools. ARPN J Eng Appl Sci 5(3):11–15
8. Miller SF, Li R, Wang H, Shih AJ (2006) Experimental and numerical analysis of the friction drilling process. J Manuf Sci Eng 128(3):802–810. https://doi.org/10.1115/1.2193554
9. Miller SF, Shih AJ (2007) Thermo-mechanical finite element modeling of the friction drilling process. J Manuf Sci Eng 129(3): 531–538. https://doi.org/10.1115/1.2716719
10. Engbert T, Heymann T, Biermann D, Zabel A (2011) Flow drilling and thread forming of continuously reinforced aluminium extrusions. Proc Inst Mech Eng B J Eng Manuf 225(3):398–407
11. Krasauskas P (2011) Experimental and statistical investigation of thermo-mechanical friction drilling process. Mechanika 17(6):681–686. https://doi.org/10.5755/j01.mech.17.6.1014
12. Özek C, Demir Z (2013) Investigate the surface roughness and bushing shape in friction drilling of A7075-T651 and St 37 steel. TEM J 2(2):170–180
13. Boopathi M, Shankar S, Manikandakumar S, Ramesh R (2013) Experimental investigation of friction drilling on brass, aluminium

and stainless steel. Procedia Eng 64:1219–1226. https://doi.org/10.1016/j.proeng.2013.09.201
14. Hannich S, Biermann D (2013) Analysis of flow drilling and thread forming regarding the angle between workpiece surface and tool axis. LightMAT 2013, Proc of International Congress and Exhibition on Light Materials, pp 1–6
15. Raju BP, Swamy MK (2012) Finite element simulation of a friction drilling process using deform-3D. Int J Eng Res App 2(6):716–721
16. Özek C, Demir Z (2013) Investigate the friction drilling of aluminium alloys according to the thermal conductivity. TEM J 2(1):93–101
17. Demir Z, Özek C (2014) Investigate the effect of pre-drilling in friction drilling of A7075-T651. Mater Manuf Process 29(5):593–599. https://doi.org/10.1080/10426914.2014.892986
18. Gopichand A, Brahmam MV, Bhanuprakash D (2014) Numerical simulation and analysis of friction drilling process for alumina alloy using Ansys. Int J Eng Res Tech 3(12):602–607
19. Wittke P, Liu Y, Biermann D, Walther F (2015) Influence of the production process on the deformation and fatigue performance of friction drilled internal threads in the aluminum alloy 6060. Mater Test 57(4):281–288. https://doi.org/10.3139/120.110712
20. Wittke P, Walther F (2016) Cyclic deformation behavior of friction drilled internal threads in AlSi10Mg and AZ31 profiles. Procedia Struct Integr 2:3264–3271. https://doi.org/10.1016/j.prostr.2016.06.407
21. Biermann D, Walther F, Hannich S, Wittke P (2017) Front face flow drilling of lightweight cast materials. Procedia Eng 207:956–961. https://doi.org/10.1016/j.proeng.2017.10.858
22. Eliseev AA, Fortuna SV, Kolubaev EA, Kalashnikova TA (2017) Microstructure modification of 2024 aluminum alloy produced by friction drilling. Materi Sci Eng A 691:121–125. https://doi.org/10.1016/j.msea.2017.03.040
23. Eliseev AA, Kalashnikova TA, Fortuna SV (2017) Microstructure evolution of AA3005 in friction drilling. AIP Conf Proc 1909(020038):1–4. https://doi.org/10.1063/1.5013719
24. Eliseev AA, Kalashnikova TA, Fortuna SV (2017) Structure of AA5056 after friction drilling. AIP Conf Proc 1909(020039):1–4. https://doi.org/10.1063/1.5013720
25. Oezkaya E, Hannich S, Biermann D (2018) Development of a three-dimensional finite element method simulation model to predict modified flow drilling tool performance. Int J Mater Form:1–14. https://doi.org/10.1007/s12289-018-1429-0
26. Kerkhofs M, Van Stappen M, D'Olieslaeger M, Quaeyhaegens C, Stals LM (1994) The performance of (Ti,Al)N-coated flowdrills. Surf Coat Technol 68/69:741–746. https://doi.org/10.1016/0257-8972(94)90247-X
27. Miller SF, Blau PJ, Shih AJ (2007) Tool wear in friction drilling. Int J Mach Tool Manu 47:1636–1645. https://doi.org/10.1016/j.ijmachtools.2006.10.009
28. Chow HM, Lee SM, Yang LD (2008) Machining characteristic study of friction drilling on AISI 304 stainless steel. J Mater Process Technol 207(1–3):180–186. https://doi.org/10.1016/j.jmatprotec.2007.12.064
29. Lee SM, Chow HM, Huang FY, Yan BH (2009) Friction drilling of austenitic stainless steel by uncoated and PVD AlCrN- and TiAlN-coated tungsten carbide tools. Int J Mach Tool Manu 49:81–88. https://doi.org/10.1016/j.ijmachtools.2008.07.012
30. Ku WL, Hung CL, Lee SM, Chow HM (2011) Optimization in thermal friction drilling for SUS 304 stainless steel. Int J Adv Manuf Technol 53(9–12):935–944. https://doi.org/10.1007/s00170-010-2899-5
31. Kaya MT, Aktas A, Beylergil B, Akyildiz HK (2014) An experimental study on friction drilling of ST12 steel. Trans Can Soc Mech Eng 38(3):319–329. https://doi.org/10.1139/tcsme-2014-0023
32. Krasauskas P, Kilikevičius S, Česnavičius R, Pačenga D (2014) Experimental analysis and numerical simulation of the stainless AISI 304 steel friction drilling process. Mechanika 20(6):590–595. https://doi.org/10.5755/j01.mech.20.6.8664
33. El-Bahloul SA, El-Shourbagy HE, El-Bahloul AM, El-Midany TT (2018) Experimental and thermo-mechanical modeling optimization of thermal friction drilling for AISI 304 stainless steel. CIRP J Manuf Sci Technol 20:84–92. https://doi.org/10.1016/j.cirpj.2017.10.001
34. Dehghan S, Ismail MIS, Ariffin MKA, Baharudin BTHT (2018) Experimental investigation on friction drilling of titanium alloy. Eng Solid Mech 6(2):135–142. https://doi.org/10.5267/j.esm.2018.2.002
35. Kumar R, Hynes NRF (2018) Numerical analysis of thermal drilling technique on titanium sheet metal. AIP Conf Proc 1953(1):130014. https://doi.org/10.1063/1.5033158
36. Lee SM, Chow HM, Yan BH (2007) Friction drilling of In-713LC cast superalloy. Mater Manuf Process 22(7):893–897
37. Biermann D, Liu Y (2014) Innovative flow drilling on magnesium wrought alloy AZ31. Procedia CIRP 18:209–214. https://doi.org/10.1016/j.procir.2014.06.133
38. Biermann D, Walther F, Hannich S, Wittke P (2017) Temperature controlled front face flow drilling of magnesium alloys. LightMAT 2017, Proc of the 2nd International Conference on Light Materials, pp 1–2
39. Zhang BP, Tu YF, Chen JY, Zhang HL, Kang YL, Suzuki HG (2007) Preparation and characterization of as-rolled AZ31 magnesium alloy sheets. J Mater Process Technol 184:102–107. https://doi.org/10.1016/j.jmatprotec.2006.11.009
40. Ebel-Wolf B, Walther F, Eifler D (2007) Cyclic deformation behaviour and lifetime calculation of the magnesium die-cast alloys AZ91D, MRI 153M and MRI 230D. Int J Mater Res 98(2):117–122. https://doi.org/10.3139/146.101443
41. Walther F (2014) Microstructure-oriented fatigue assessment of construction materials and joints using short-time load increase procedure. Mater Test 56(7–8):519–527. https://doi.org/10.3139/120.110592
42. Corby C, Cáceres CH, Lukáč P (2004) Serrated flow in magnesium alloy AZ91. Mat Sci Eng A 387–389:22–24. https://doi.org/10.1016/j.msea.2004.01.077
43. Trojanová Z, Cáceres CH, Lukáč P, Čížek L (2008) Serrated flow in AZ91 magnesium alloy in tension and compression. Kovove Mater 46(5):249–256
44. Goodenberger DL, Stephens RI (2008) Fatigue of AZ91E-T6 cast magnesium alloy. J Eng Mater Technol 115(4):391–397. https://doi.org/10.1115/1.2904236
45. Eisenmeier G, Holzwarth B, Höppel HW, Mughrabi H (2001) Cyclic deformation and fatigue behaviour of the magnesium alloy AZ91. Mat Sci Eng A 319-321:578–582. https://doi.org/10.1016/S0921-5093(01)01105-4